PERGAMON

International Journal of Heat and Mass Transfer 44 (2001) 2739–2750

International Journal of HEAT and MASS TRANSFER

www.elsevier.com/locate/ijhmt

Effect of centrifugal buoyancy on turbulent heat transfer in an orthogonally rotating square duct with transverse or angled rib turbulators

Akira Murata [a,*], Sadanari Mochizuki [b]

[a] *Graduate School of Bio-Applications and Systems Engineering, Tokyo University of Agriculture and Technology, 2-24-16 Nakacho, Koganei, Tokyo 184-8588, Japan*

[b] *Department of Mechanical Systems Engineering, College of Engineering, Tokyo University of Agriculture and Technology, 2-24-16 Nakacho, Koganei, Tokyo 184-8588, Japan*

Received 16 December 1999; received in revised form 10 August 2000

Abstract

The effect of the Coriolis and buoyancy forces on the turbulent heat transfer disturbed by rib turbulators was numerically investigated by using the large eddy simulation (LES). The computational condition was as follows: the turbulent Reynolds number of 350, the rotation number of 1.0, the rib angles of 90° and 60°, and the Rayleigh number from -5×10^4 to $+5 \times 10^4$. The heat transfer was enhanced and suppressed by the buoyancy-induced aiding and opposing flows, respectively. The friction factor was dominated by the form drag, and the results of 90° and 60° rib showed different behavior for the Rayleigh number change. © 2001 Published by Elsevier Science Ltd.

1. Introduction

In the development of high performance gas turbines, effective blade cooling is essential because the higher efficiency of the turbine requires a higher inlet gas temperature. Generally, this blade cooling is performed by film cooling at the external surface of the turbine blade and also by internal forced-convection cooling which uses winding flow passages inside the turbine blade. In the internal forced-convection cooling, the real phenomena are very complicated due to external forces: the Coriolis force and the buoyancy force in the centrifugal acceleration field. In addition to these external forces, the effects induced by a 180° sharp turn and turbulence promoters (ribs) installed on the thermally severe opposing internal-surfaces result in phenomena that are far from understood [1].

As for the local heat transfer of a rib-roughened duct, several researchers investigated the spatial variation of the local heat transfer with various techniques: wall temperature measurement by using thermocouples [2–4], the naphthalene sublimation technique [5,6], and wall temperature measurement by using temperature-sensitive liquid crystal [7–9]. In these studies, the heat transfer variation induced by the flow separation and reattachment behind the rib was captured to a certain extent. However, it is difficult to perform experiments in a rotating condition which can identify the flow structure and its influence on the heat transfer. Thus, further progress in experimental studies has so far been prevented.

In previous numerical studies of rib-roughened ducts, the Reynolds-averaged Navier–Stokes equation with a turbulence model was solved for transverse [10] and angled [11,12] rib configurations. Launder et al. [13] pointed out that in order to quantitatively simulate the flow in a rotating system, the second moment closure, that is, the Reynolds stress equation model, is a minimum requirement considering a non-isotropic effect of the Coriolis force on turbulence. Although this approach

* Corresponding author. Tel.: +81-42-388-7089; fax: +81-42-385-7204.

E-mail address: murata@mmlab.mech.tuat.ac.jp (A. Murata).

0017-9310/01/$ - see front matter © 2001 Published by Elsevier Science Ltd.
PII: S0017-9310(00)00313-6

Nomenclature

c_p	specific heat, J/(kg K)
C_S	Smagorinsky constant
D	side length of square duct (= hydraulic diameter), m
e	side length of ribs, m
f	friction factor ($= \Delta p/(2\rho U_m^2)$)
F_i	external force term
Gr_*	Grashof number ($= \beta T_r \omega^2 r_m \ell^3/\nu^2$)
Gr_m	Grashof number ($= \beta \dot{q} \omega^2 r_m^4/(\nu^2 \lambda)$)
h	heat transfer coefficient, W/(m^2 K)
H_0	dimensionless distance between rotation axis and duct entrance ($= H_{0\,dim}/\ell$)
$H_{0\,dim}$	distance between rotation axis and duct entrance ($z = 0$), m
j	Colburn's j factor ($= Nu_m/(Re_m Pr^{1/3})$)
k	dimensionless turbulent kinetic energy normalized by u_*^2
ℓ	length scale ($= 0.5D$), m
L_p	peripheral location normalized by ℓ
Nu	Nusselt number ($= hD/\lambda$)
Δp	pressure loss in streamwise length D, Pa
P	rib pitch ($= D$), m
Pr	Prandtl number ($= 0.71$)
Pr_{SGS}	Prandtl number of subgrid-scale model ($= 0.5$)
$\dot{q}$	wall heat flux, W/m^2
r_m	mean rotation radius, m
R_m	dimensionless mean rotation radius ($= r_m/\ell$)
Ra_*	Rayleigh number ($= Gr_* Pr$)
Re_m	Reynolds number ($= U_m D/\nu$)
Re_*	turbulent Reynolds number ($= u_* \ell/\nu$)
Ro_m	rotation number ($= \omega D/U_m$)
Ro_*	rotation number ($= \omega \ell/u_*$)
S_{ij}	rate-of-strain tensor
t	dimensionless time normalized by ℓ/u_*
T	temperature, K
T_b	bulk temperature, K
T_r	friction temperature ($= \dot{q}/(\rho c_p u_*)$), K
T_∞	reference temperature, K
u, v, w	dimensionless velocities in x, y, z directions normalized by u_*
u_*	mean friction velocity, m/s
U_m	mean velocity, m/s
x, y, z	coordinates in transverse, vertical, streamwise directions normalized by ℓ
$\Delta x, \Delta y, \Delta z$	grid spacing in x, y, z directions normalized by ℓ
$\alpha_{SGS\ j}$	subgrid-scale energy flux
β	expansion coefficient, 1/K
γ	rib angle, deg
λ	thermal conductivity, W/(mK)
ν	kinematic viscosity, m^2/s
ν_{SGS}	dimensionless subgrid-scale eddy viscosity normalized by $u_* \ell$
ω	angular velocity, rad/s
ρ	density, kg/m^3
θ	dimensionless temperature ($= (T - T_b)/T_r$)
θ_∞	dimensionless reference temperature
$\tau_{SGS\ ij}$	subgrid-scale stress tensor
τ_w	streamwise component of wall shear stress, Pa
ξ, η, ζ	curvilinear coordinates normalized for grid spacing to become unity

Superscripts and subscripts

B	Blasius
L	local value
m	duct average or based on mean velocity
w	wall
∞	fully developed or reference value
$*$	friction velocity or defined by using u_*
$+$	dimensionless value based on inner scales (normalized by ν/u_* for length and ν/u_*^2 for time)
$-$	grid resolvable component or turbulent statistical value
$'$	fluctuating component

using the Reynolds-averaged turbulence model could reproduce the heat transfer of blade cooling to a certain extent, even the Reynolds stress equation model has empirical constants and functions which have to be adjusted depending on the flow field, and therefore the applicability of the model should carefully be examined. Recent advancement in computers enables us to numerically simulate the fluctuating components of the turbulent flow by using the large eddy simulation (LES) or the direct numerical simulation (DNS). Because LES and DNS directly resolve temporal variation of the fluctuating components, the results are more universal, in other words, more free from the empirical modeling than the Reynolds-averaged turbulence models. So far, the turbulent flow in a stationary smooth duct with a square cross-section was solved using DNS [14,15] and LES [16,17].

The authors' group has performed heat transfer measurements by using thermocouples in both stationary and rotating conditions [2–4]. Recently, numerical analyses were also performed by using a dynamic subgrid-scale model for a rotating smooth duct of which

cross-section was square [18] and rectangular [19], and the technique was further applied to a rotating transversely rib-roughened duct [20,21]. In our previous numerical results, the followings were examined and clarified: the effect of duct cross-sectional aspect ratio on the Coriolis induced secondary flow, the dissimilarity between the velocity and temperature fields induced by the flow separation and reattachment, and the very high heat transfer area located in front of the ribs which was caused by the unsteady movement of the separation bubbles there. Very recently, further investigation was performed for the angled rib effect on the heat transfer in a straight square duct using a coordinate system fitted to the angled ribs [22,23]. Although the effect of the buoyancy force in the centrifugal acceleration field is very important considering the highly severe thermal condition with high rotation rate to which the real turbine blades are exposed, the buoyancy effect was ignored in our previous studies.

This study examines the effect of the centrifugal buoyancy on the flow and heat transfer which are at the same time influenced by the secondary flows induced by the Coriolis force and the angled ribs. The LES was performed by changing the Rayleigh number for two different rib angles of 90° and 60°; the simulation was performed for both radially inward and outward flow configurations because the relative direction between the main flow and the centrifugal buoyancy changes depending on the radial flow direction.

2. Numerical analysis

Fig. 1 shows the computational domain and coordinate system used in this study. The duct had a square cross-section with a side length of D which is the hydraulic diameter. The coordinate system was fixed to a rotating duct which had an angular velocity of ω. The streamwise (radially outward) direction was chosen in the z-direction; the x- and y-directions were transverse and perpendicular directions to rib-roughened walls,

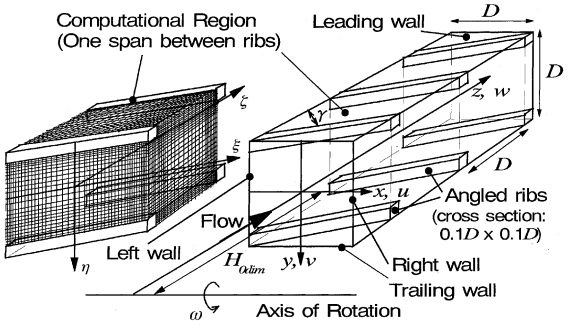

Fig. 1. Schematic of a rotating rib-roughened duct and a grid system fitted to angled ribs.

respectively. Ribs were installed on trailing and leading walls with the rib angle, γ. In this study, the cases of $\gamma = 90°$ and 60° were computed. By assuming the periodicity of the flow field with respect to the streamwisely repeated ribs, streamwise one span was chosen for the computational domain. The cross-section of the rib was square (side length $e = 0.1D$), and streamwise pitch, P, was set equal to the hydraulic diameter, $P = D$. This rib arrangement gave the rib height-to-hydraulic diameter ratio of 0.1 and the rib pitch-to-rib height ratio of 10. This rib arrangement was chosen because it was within the previously reported optimal range [24,25]. The rib angle, 60°, was chosen as the angle which gave the maximum heat transfer in the study of Han et al. [26].

The present procedure of the numerical analysis is the same as our recent studies [22,23] which is the extension of our procedure in the Cartesian coordinate system [18–21] to the generalized curvilinear coordinate system. After applying a filtering operation to the incompressible Navier–Stokes equation with a filter width equal to the grid spacing [16], the dimensionless governing equations scaled by a length scale, ℓ $(= 0.5D)$, and mean friction velocity, u_*, became a set of dimensionless governing equations with respect to grid resolvable components indicated by overbars as $(\bar{u}, \bar{v}, \bar{w})$ under the assumption of constant fluid properties. In order to simulate a fully developed situation, the pressure and temperature fields were decomposed into the steady and streamwisely linear component and the remaining component [27]. By this decomposition, the pressure and temperature fields became periodic in the streamwise direction. The temperature was made dimensionless by using a bulk temperature, T_b, and a friction temperature, T_r, as $\theta = (T - T_b)/T_r$. Accordingly, the dimensionless energy equation was derived for the grid resolvable component, $\bar{\theta}$. An external force term of the momentum equations, F_i, had the Coriolis force, the centrifugal buoyancy force with the Boussinesq approximation, and the mean pressure gradient term with a value of two as follows:

$$F_i = \begin{pmatrix} 0 \\ 2Ro_*\bar{w} - \dfrac{Gr_*}{Re_*^2}\dfrac{(\bar{\theta} - \bar{\theta}_\infty)y}{R_m} \\ -2Ro_*\bar{v} - \dfrac{Gr_*}{Re_*^2}\dfrac{(\bar{\theta} - \bar{\theta}_\infty)}{R_m}(H_0 + z) + 2 \end{pmatrix}. \quad (1)$$

Because the mean pressure gradient which drove the flow in the streamwise direction was set to be constant in this study, the flow rate varied depending on the flow conditions (rib angle and the Rayleigh number); therefore, the flow rate was not known a priori, and the flow rate was calculated from the resultant computed flow field after the fully developed condition was attained. Because the dimensionless mean rotation radius, R_m, is much larger than y and z in the real gas turbines, the following approximation can be used: $y/R_m \fallingdotseq 0$ and

$(H_0+z)/R_m \fallingdotseq 1$. In the dimensionless reference temperature, $\theta_\infty = (T_\infty - T_b)/T_r, T_b$ changes linearly with respect to z, and therefore $\bar{\theta}_\infty$ also changes linearly with respect to z. This effect of $\bar{\theta}_\infty$ was included in the pressure term, and consequently Eq. (1) was approximated as follows:

$$F_i = \begin{pmatrix} 0 \\ 2Ro_*\bar{w} \\ -2Ro_*\bar{v} - \dfrac{Gr_*}{Re_*^2}\bar{\theta} + 2 \end{pmatrix}. \tag{2}$$

The relative direction between the main flow and the centrifugal buoyancy changes depending on the radial flow direction: radially inward and outward flows. In this study, instead of changing the main flow direction, the relative direction between the main flow and the buoyancy was simulated by changing the sign of the Grashof number, Gr_*, in Eq. (2): the positive and negative values of Gr_* corresponded to the radially outward and inward flows, respectively. This procedure was adopted because in this case the pressure and suction surfaces with respect to the Coriolis induced secondary flow always corresponded to the trailing and leading walls, respectively. Therefore, when the present numerical results are compared with experimental results of the radially inward flow, note that the present trailing and leading walls for negative Gr_* correspond to the leading and trailing walls of the experiments.

In order to adopt the coordinate system fitted to the angled ribs, the governing equations in the Cartesian coordinates (x,y,z) were transformed into generalized curvilinear coordinates (ξ,η,ζ) [28]. Subgrid-scale components of stress, $\tau_{SGS\,ij}$, and energy flux, $\alpha_{SGS\,j}$, were expressed as follows:

$$\tau_{SGS\,ij} = 2\nu_{SGS}\bar{S}_{ij}, \tag{3}$$

$$\alpha_{SGS\,j} = \frac{\nu_{SGS}}{Pr_{SGS}}\frac{\partial\xi^k}{\partial x_j}\frac{\partial\bar{\theta}}{\partial\xi^k}, \tag{4}$$

where

$$\bar{S}_{ij} = \frac{1}{2}\left(\frac{\partial\xi^k}{\partial x_j}\frac{\partial\bar{u}_i}{\partial\xi^k} + \frac{\partial\xi^k}{\partial x_i}\frac{\partial\bar{u}_j}{\partial\xi^k}\right), \tag{5}$$

$$\nu_{SGS} = C_S^2(\Delta x\Delta y\Delta z)^{2/3}\sqrt{2\bar{S}_{ij}\bar{S}_{ij}}. \tag{6}$$

The angled rib case has no geometric symmetry in the transverse direction, and therefore we adopted the Lagrangian dynamic subgrid-scale model of Meneveau et al. [29] which averaged the value of C_S along the streamline for a certain distance. This Lagrangian dynamic subgrid-scale model was also applied to the 90° rib case. The turbulent Prandtl number for the subgrid-scale component, Pr_{SGS}, was set to 0.5 [30]. The width of the test filter was double the grid spacing, and the space filter was accurate to fourth order.

Discretization was performed by a finite difference method using the collocated grid system [28]. The spatial and temporal discretization schemes were similar to those of [15]: the second order central differencing method and the Crank–Nicolson method for the viscous term, and the second order differencing method satisfying the conservative property and the second order Adams–Bashforth method for the convective term. The external force term was also treated by the second order Adams–Bashforth method. The pressure field was treated following the MAC method [31], and the algebraic equation for each variable was solved by using the SOR method. The computational domain was one span between streamwise consecutive ribs (see Fig. 1), and its dimension was $2\times2\times2$ in x,y,z directions, respectively. This can be expressed as $700\times700\times700$ when made dimensionless by using an inner length scale, ν/u_*.

The turbulent Reynolds number, Re_* $(=u_*\ell/\nu)$, was 350, the rotation number $(=\omega\ell/u_*)$ was 1.0, and the Rayleigh number was varied in $Ra_* = -5\times10^4$ to $+5\times10^4$. Table 1 summarizes the conversion of dimensionless numbers defined by the mean friction velocity and $0.5D$ to those defined by the mean velocity and D. The range of Ra_* for which the converged results were obtained was affected by the rib angle. As explained above, the value of Re_m was calculated from the result of computation; Re_m was not known a priori. At the wall boundary, no-slip and constant heat flux conditions were imposed, although the rib side surfaces were set to

Table 1
Dimensionless number range (Re_*, Ro_*, Ra_*) of this study and its conversion into the conventional form (Re_m, Ro_m, Gr_m)

Rib angle	Re_*	Ro_*	Ra_*	Re_m	Ro_m	Gr_m
90°		1.0	$+10^4$	3360	0.417	$+5.6\times10^7$
			0	3829	0.366	0
			-10^4	4238	0.330	-5.6×10^7
60°		1.0	$+5\times10^4$	3753	0.373	$+2.8\times10^8$
	350		0	3654	0.383	0
			-5×10^4	2545	0.550	-2.8×10^8
Smooth		2.0	$+10^3$	8441	0.332	$+5.6\times10^6$
			0	9043	0.310	0
			-10^3	9510	0.294	-5.6×10^6

be adiabatic. This adiabatic condition was adopted to preserve the linear increase of the bulk temperature and also to consider the previous experiments in which the ribs were not heated. An additional computation with the constant heat flux condition at the rib side surfaces was also performed, and it was confirmed that even when the rib side surfaces were heated, the conclusions of this study were not changed. At the inlet and outlet boundaries, the periodic boundary condition [27] was imposed in order to obtain a fully developed flow. The boundary conditions of the intermediate velocities and the pressure were set following the procedure of [32] and [33].

The grids in the physical domain were contracted to both the walls and the rib surfaces by using a tangent hyperbolic function (see Fig. 1). The grid number was $47 \times 47 \times 47$, and this grid configuration gave a grid spacing of $\Delta x^+ = 1.0$ to 38, $\Delta y^+ = 0.6$ to 52, and $\Delta z^+ = 4.0$ to 28. The effect of the grid spacing on the computed result was checked by increasing the grid number to $65 \times 65 \times 65$ for several cases, and no major difference was observed. The verification of the present computational procedure was also performed for the straight smooth duct as was performed in [18], and the agreement with the previous DNS results [14,15] for the straight smooth square duct in the stationary condition was almost the same as that seen in [18]: the comparison was made in the mean velocity profile, the three components of the turbulence intensities, and the secondary flow intensity of the Prandtl's second kind.

The time step interval was $\Delta t = 1.0 \times 10^{-4}$, which can be expressed as $\Delta t^+ = 0.035$ when made dimensionless by an inner time scale, v/u_*^2. The computation was started using the result of the similar condition as an initial condition. The calculations were carried out to 160,000 steps to fully develop the flow. After the initial 160,000 steps were performed, additional 80,000 steps ($t = 8$ or $t^+ = 2800$) were performed for computing the statistical values of the turbulent flow. This 80,000-step computation needed about 15 CPU hours using an NEC SX4B. As for the cases without the buoyancy, the previous data [21,22] of 400,000 steps were used. For comparison, the smooth duct case was also computed by using the same fourth order scheme as [18] and [19] in the physical domain of $2 \times 2 \times 12$ (x, y, z directions) with $65 \times 65 \times 65$ grid points. For this smooth duct case, the case of $Re_* = 350$ and $Ro_* = 2.0$ (see Table 1) was computed with $\Delta t = 0.5 \times 10^{-3}$, and the 20,000 steps were computed for the statistical values after fully developed flow was attained.

3. Results and discussion

Before examining the results of the rotating cases, the result of the stationary case [23] was compared with the previous experimental results in Table 2. The Nusselt number was normalized using the following empirical correlation for a fully developed pipe flow [34]:

$$Nu_\infty = 0.022\, Re_m^{0.8}\, Pr^{0.5}. \tag{7}$$

The wall-averaged Nusselt number, Nu_w/Nu_∞, of the stationary case ($Ro_* = 0$) agreed with the experimental results of Chandra et al. [5] and Rau et al. [7]. However, it should be noted that the experimental condition differs from the computational condition, and the spatial resolution in the experiments of Chandra et al. [5] is low: three locations in the transverse direction.

Fig. 2 shows the streamwise component of the wall shear stress (left figures) and the local Nusselt number (right figures) on the four walls for the 90° rib case. In the figures, out-of-range values are shown by white and black solid areas for very low and very high values, respectively. For easier understanding of the figures, the sign of the wall shear stress ($(+), (-)$) and the level of the Nusselt number (high, low) are added to the figures of $Ra_* = 0$ (Fig. 2(b)).

The results of Figs. 2(a) and (c) are less symmetric than that of Fig. 2(b), because the cases with buoyancy (Figs. 2(a) and (c)) are averaged for 80,000 steps, which is one-fifth of the sample size for the cases without buoyancy (Fig. 2(b): 400,000 steps). The effect of this reduced total time step was discussed in [21], and it was verified that the wall- and duct-averaged values did not show a major difference even when the sample size was as small as 40,000 steps. As explained in the previous study [21], when there is no buoyancy force ($Ra_* = 0$) in Fig. 2(b), on the trailing wall, the heat transfer behind the ribs is for a time low due to the flow separation, and it then takes a local maximum at the midpoint between

Table 2
Comparison between the present wall-averaged Nusselt number, Nu_w/Nu_∞, and the previous experimental results for the stationary condition, $Ro_* = 0$ (the experimental result of Chandra et al. [5] is for $Re_m = 30,000$, $e/D = 0.063$, and $P/e = 10$; that of Rau et al. [7] is for $Re_m = 30,000$, $e/D = 0.1$, and $P/e = 10$)

	90° rib		60° rib		
	Ribbed wall	Side wall	Ribbed wall	Left wall	Right wall
Present results	2.2	2.0	3.4	2.8	3.0
Chandra et al. [5]	2.6	1.8	3.3	2.2	2.2
Rau et al. [7]	2.4	2.1	–	–	–

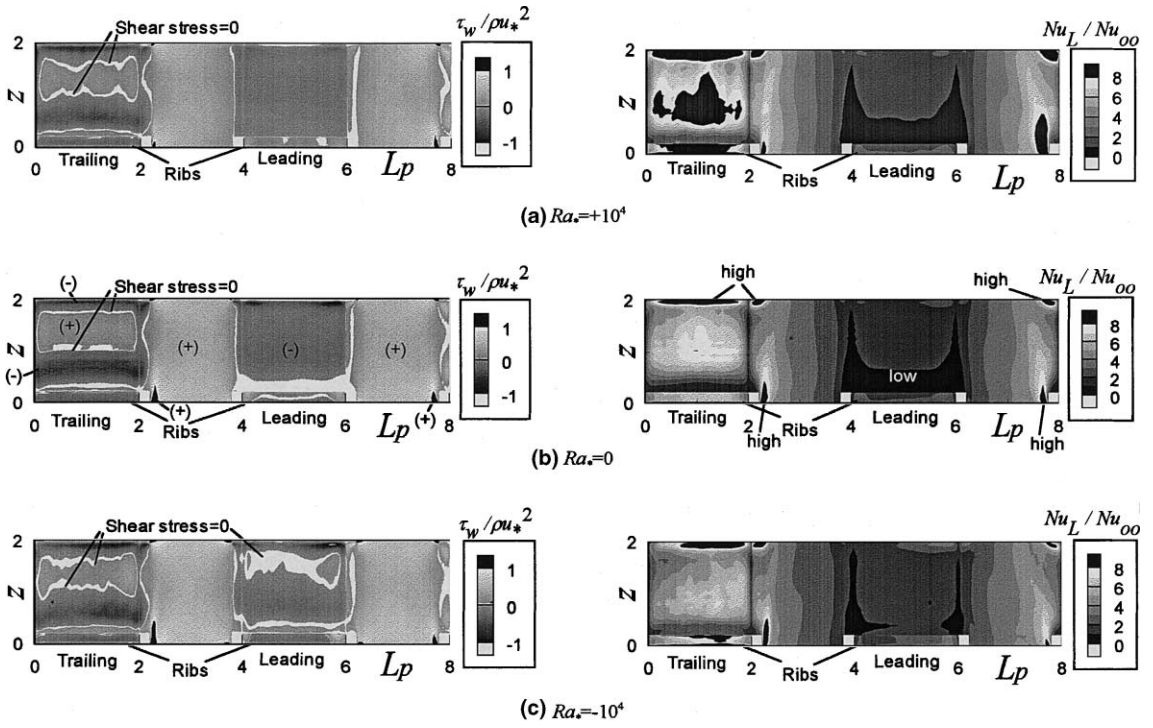

Fig. 2. Spatial variation of time-averaged streamwise wall shear stress (left) and Nusselt number (right) on four walls for various Ra_* (90° rib and $Ro_* = 1$).

the ribs due to the flow reattachment; in front of the ribs, the high heat transfer area correlated with the negative wall shear stress is formed. As explained in Fig. 3, because of the Coriolis induced secondary flow, the fluid temperature on the trailing side becomes lower than that on the leading side [21]; therefore, on the trailing side, the positive (Fig. 2(a)) and negative (Fig. 2(c)) values of Ra_* correspond to the aiding and opposing flows, respectively. In the aiding flow, the directions of the main flow and the buoyancy force on the low temperature fluid are same; on the other hand, in the opposing flow, the directions become opposite. Therefore, the increase

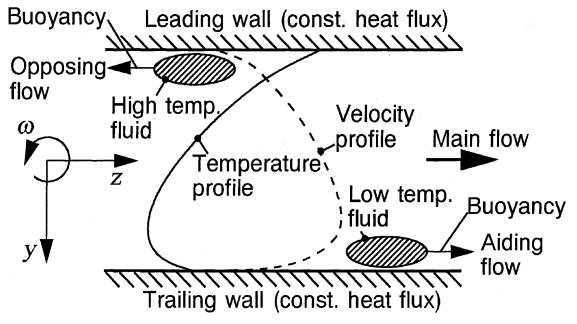

Fig. 3. Explanation of aiding and opposing flows for radially outward flow configuration ($Ra_* > 0$).

of Ra_* induces the increase of the heat transfer on the trailing wall. On the other hand, on the leading wall, due to the high fluid temperature [21], the positive and negative values of Ra_* correspond to the opposing and aiding flows, respectively. The situation is reversed to the trailing wall case: the decrease of Ra_* induces the increase of the heat transfer on the leading wall. Moreover, the aiding flow on the leading wall forms a weak flow reattachment as can be deduced from the zero wall shear stress area at the downstream area between the ribs (Fig. 2(c) left). It should be noted that the definition of the aiding and opposing flows in this study is different from that of Nishimura and Kasagi [35] in which the high and low temperature walls were used in a rotating flow passage between two parallel plates. In this study, the walls have uniform heat flux, and therefore the fluid in the vicinity of the walls is always heated. Following the definition of Nishimura and Kasagi [35], irrespective of the pressure and suction surfaces, the positive and negative values of Ra_* correspond to the opposing and aiding flows, respectively.

In Fig. 4, the streamwise component of the wall shear stress and the Nusselt number are shown for the 60° rib case. The notches around the ribs are caused by the inadequate interpolation ability of the software used in drawing the figure, and the numerical results themselves do not oscillate. Here again, for easier understanding of

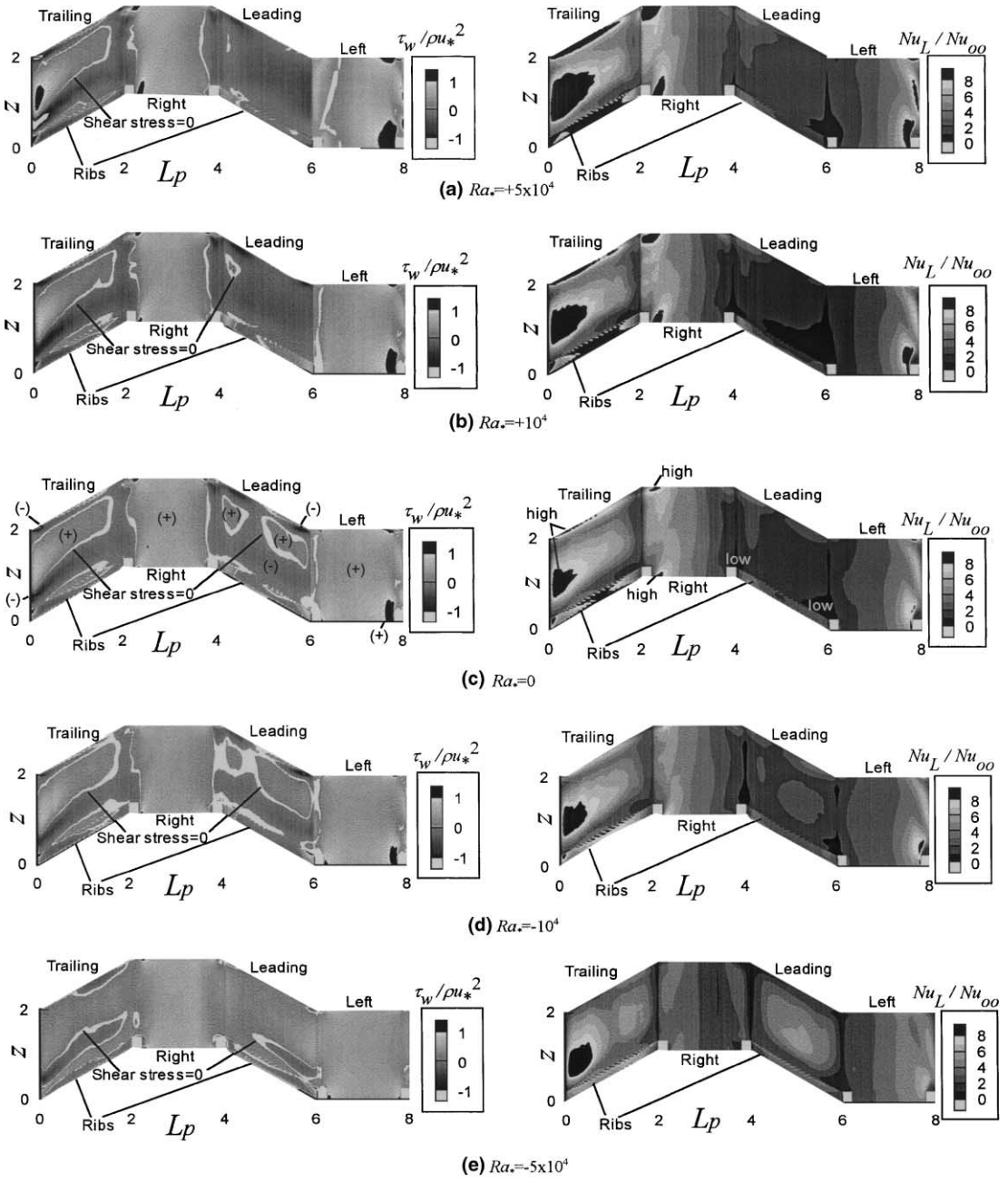

Fig. 4. Spatial variation of time-averaged streamwise wall shear stress (left) and Nusselt number (right) on four walls for various Ra_* (60° rib and $Ro_* = 1$).

the figures, the sign of the wall shear stress ($(+), (-)$) and the level of the Nusselt number (high, low) are added to the figures of $Ra_* = 0$ (Fig. 4(c)). For $Ra_* = 0$ of Fig. 4(c) [22], both the wall shear stress and the heat transfer are higher on the trailing side than those on the leading side. On the trailing wall, the high heat transfer area at the midpoint between the ribs is shifted to the left wall due to the angled-rib induced secondary flow, and this area is correlated with the positive wall shear stress. In front of the ribs, another high heat transfer area is seen which is correlated with the negative wall shear stress, and this area is also shifted to the left wall. On the smooth side walls, the values around the trailing ribs are higher on the left wall than those on the right wall. On

the other hand, on the right wall, the Nusselt number becomes high in the wider area than that on the left wall.

As explained in the 90° rib case of Fig. 2, the positive and negative values of Ra_* on the trailing wall correspond to the aiding and opposing flows, respectively; on the leading wall, the relation is reversed. In the 60° rib case of Fig. 4, the increase of Ra_* induces the increase of the wall shear stress and the Nusselt number on the trailing wall; on the other hand, it induces the decrease of those values on the leading wall. The dependency of the 60° rib result on Ra_* is similar to that of the 90° rib result.

Figs. 5–7 show the effect of the centrifugal buoyancy on the wall-averaged Nusselt number, Nu_w, and the friction factor, f. In the figures, the effect of the buoyancy is expressed by using the Grashof number, Gr_m, which is often used in correlating the experimental results. The following relation holds due to the definition of Gr_m:

$$Gr_m = 16Re_*Pr, Gr_* = 16Re_*Ra_*. \quad (8)$$

The values of Nu_w and f were normalized by using Nu_∞ of Eq. (7) and f_B of the Blasius equation as follows:

$$f_B = 0.079Re_m^{-0.25}. \quad (9)$$

In the 90° rib case of Fig. 5, f and Nu_w on the trailing wall increase with the increase of Gr_m; on the other hand, Nu_w on the leading wall slightly decreases with the increase of Gr_m. Fig. 6 shows the result of the smooth square duct for comparison. Although the range of Gr_m is different between Figs. 5 and 6, the tendency agrees with each other, and it also qualitatively agrees with the experimental results of Wagner et al. [36] and Johnson et al. [37] for the rotating smooth and 90° rib-roughened

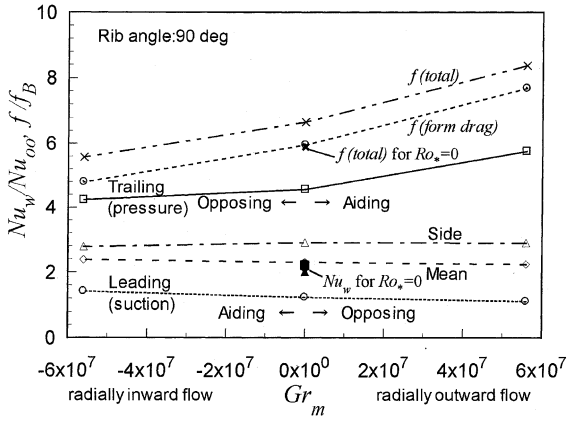

Fig. 5. Effect of the buoyancy force on the wall-averaged Nusselt number and the friction factor (90° rib case; $Ro_* = 1$ except the filled or bold symbols at $Gr_m = 0$ which are for stationary condition ($Ro_* = 0$)).

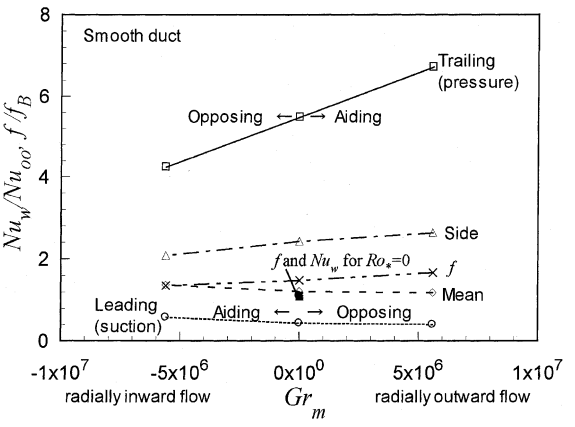

Fig. 6. Effect of the buoyancy force on the wall-averaged Nusselt number and the friction factor (smooth duct case; $Ro_* = 2$ except the filled or bold symbols at $Gr_m = 0$ which are for stationary condition ($Ro_* = 0$)).

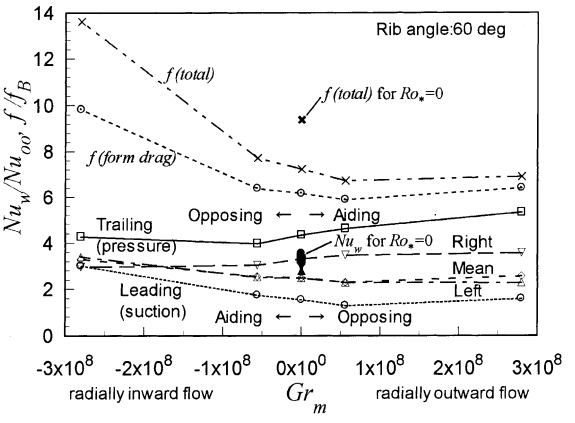

Fig. 7. Effect of the buoyancy force on the wall-averaged Nusselt number and the friction factor (60° rib case; $Ro_* = 1$ except the filled or bold symbols at $Gr_m = 0$ which are for stationary condition ($Ro_* = 0$)).

ducts. In the DNS result of Nishimura and Kasagi [35] for the rotating two-dimensional channel flow, the effect of the centrifugal buoyancy does not necessarily show the increase and decrease for the aiding and opposing flows, respectively. In addition to the above-mentioned difference in the definition of the aiding and opposing flows, the square duct flow becomes different from the two-dimensional channel flow due to the existence of the side wall. In the rotating duct case, the side wall forms the velocity distribution in the transverse direction, and this intensifies the Coriolis induced secondary flow; consequently, the friction factor and the heat transfer are highly affected by the Coriolis induced secondary flow [19]. Therefore, the result of the present square duct shows the different tendency from that of the two-di-

mensional channel where the buoyancy mainly affects the flow via the turbulent production.

The pressure loss of the rib-roughened duct consists of the skin friction on the wall and the form drag which is caused by the pressure difference on the upstream and downstream surfaces of the rib [7]. In Fig. 5, this form drag contribution is also plotted, which was calculated by subtracting the integral streamwise component of the wall shear stress from the total pressure loss. In the 90° rib case, the contribution of the form drag is dominating the pressure loss.

In the 60° rib case of Fig. 7, f decreases with the increase of Gr_m, which is opposite to the results of the 90° rib-roughened and smooth ducts. The contribution of the form drag is also very high, and the variation of f coincides with that of the form drag component. Although, in some Gr_m regions of Figs. 5 and 7, the difference between $f(\text{total})/f_B$ and $f(\text{form drag})/f_B$ becomes less than unity, it is physically understandable by considering the flow separation behind the ribs and the negative contribution to the streamwise skin friction there (see Figs. 2 and 4). The tendency of Nu_w almost agrees with that of the 90° rib except the slight increase with the increase of the absolute Gr_m seen both on the trailing and leading walls for the opposing flow in the large absolute Gr_m region.

When the influence of Gr_m on Nu_w of the trailing wall is compared between the smooth and rib-roughened ducts in Figs. 5–7, the change of the smooth duct case is slightly larger in spite of the smaller Gr_m range: one to two orders smaller than that of the rib-roughened cases. This higher sensitivity of the smooth duct case to Gr_m can be explained by the lack of disturbance caused by the ribs; the buoyancy directly and solely affects the flow and heat transfer of the smooth duct case as compared to the rib-roughened duct cases in which the flow and heat transfer are mainly affected by the rib induced secondary flow and the buoyancy effect appears through the modification of the rib induced secondary flow.

In order to examine the reason for the opposite dependency of the friction factor, f, on Gr_m between the 60° rib case and the cases of the 90° rib-roughened and smooth ducts, the time-averaged velocity vectors $(\bar{u}, \bar{v})$ of the secondary flow are shown in Fig. 8 for the 60° rib case. In Fig. 8(a) of the radially outward flow configuration, the aiding flow near the trailing wall enhances the flow passing along the angled rib from left to right in the figure, and as a result it enhances the

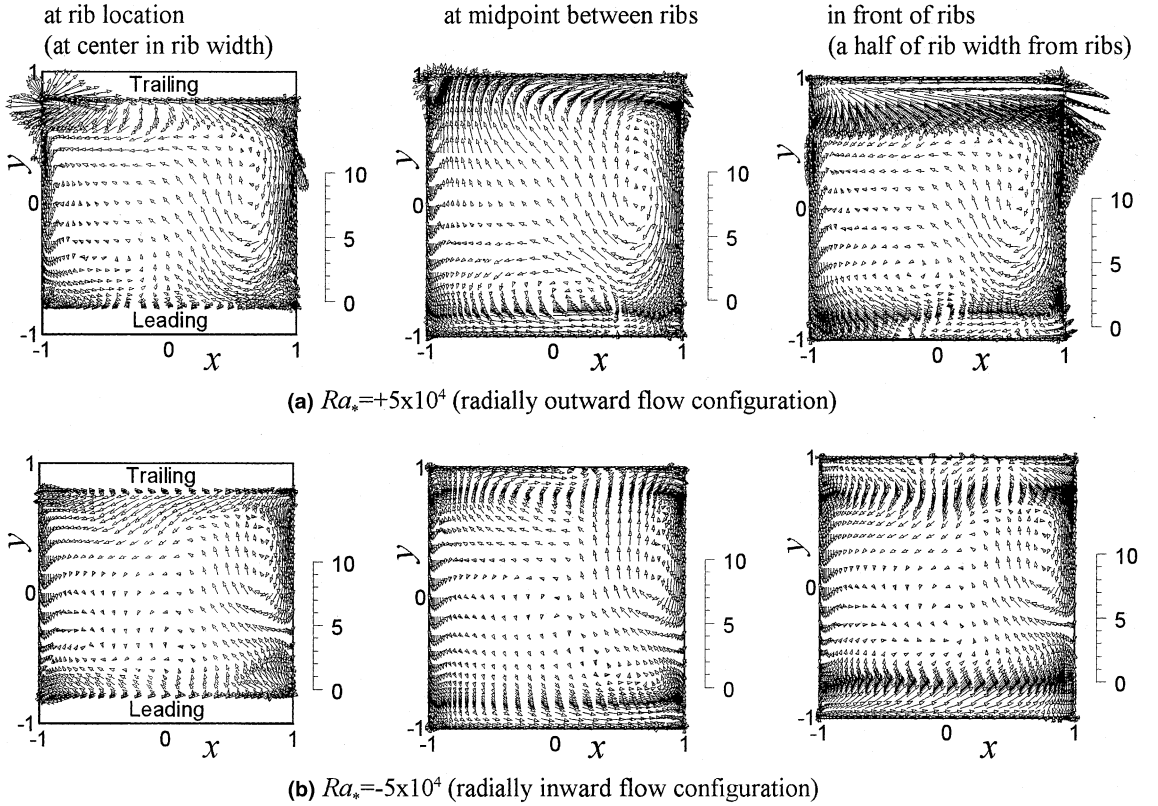

Fig. 8. Time-averaged velocity vectors $(\bar{u}, \bar{v})$ in ξ–η plane at three different streamwise locations (60° rib and $Ro_* = 1$; figures are projected onto x–y plane. The scale in each figure indicates the vector magnitude).

secondary flow induced by the Coriolis force. On the other hand, in Fig. 8(b) of the radially inward flow configuration, the aiding flow occurs near the leading wall, and it enhances the flow passing along the angled rib on the leading wall, which reverses the flow at the lower right corner as clearly seen in the comparison between Figs. 8(a) and (b). At the same time, the opposing flow near the trailing wall weakens the flow passing along the angled rib on the trailing wall in Fig. 8(b). The different secondary flows induce the different profiles in the streamwise velocity, $\bar{\omega}$, and temperature, $\bar{\theta}$: the time-averaged profiles at the midpoint between the ribs are shown in Fig. 9. In the figure, the turbulent statistical values calculated from grid-resolvable components are also shown: the turbulent kinetic energy, k, the Reynolds stress, $-\overline{v'w'}$, and the turbulent heat flux, $\overline{v'\theta'}$. The values of $-\overline{v'w'}$ and $\overline{v'\theta'}$ are chosen because these are supposed to have a dominant contribution to the turbulent transport near the rib-roughened walls. The similarity between k and $-\overline{v'w'}$ holds well. On the other hand, the similarity between $-\overline{v'w'}$ and $\overline{v'\theta'}$ breaks near the trailing wall (upper wall) for the radially outward flow configuration in Fig. 9(a), and it breaks in most area of the radially inward flow configuration in Fig. 9(b); the areas where the similarity breaks correspond to the areas where the similarity between $\overline{w}$ and $\bar{\theta}$ breaks. Although the figures are not shown, in the cases of the 90° rib-roughened and smooth ducts, the influence of the buoyancy on these variables is much smaller than the 60° rib case. In the 60° rib case, the introduction of the duct rotation induces the decrease of f as compared to the stationary case (see Fig. 7), although the 90° rib-roughened and smooth ducts show the increase of f by the rotation (see Figs. 5 and 6). As explained in Fig. 8, the case of the positive Gr_m (or Ra_*) enhances the secondary flow induced by the rotation; on the other hand, the case of the negative Gr_m suppresses it. It can be said that the resultant secondary flow for the negative Gr_m becomes closer to that of the stationary case in which both ribs on the opposing walls equally contribute to the angled-rib induced secondary flow. This difference in the secondary flow seems to give the decrease and increase of f for the positive and negative Gr_m values, respectively, and to be the reason for the larger influence of the buoyancy in the 60° rib case.

4. Conclusions

The effect of the centrifugal buoyancy in the rotating rib-roughened duct was seen in the increase and decrease of both the wall shear stress and the heat transfer for the buoyancy-induced aiding and opposing flows, respectively. The main characteristics of the fluid flow and heat transfer of the rotating rib-roughened duct for $Gr_m = 0$ (without buoyancy) were almost maintained within the present Gr_m range: the higher values on the trailing (pressure) side as compared to the leading (suction) side due to the Coriolis induced secondary flow and the high-heat-transfer spots at the midpoint

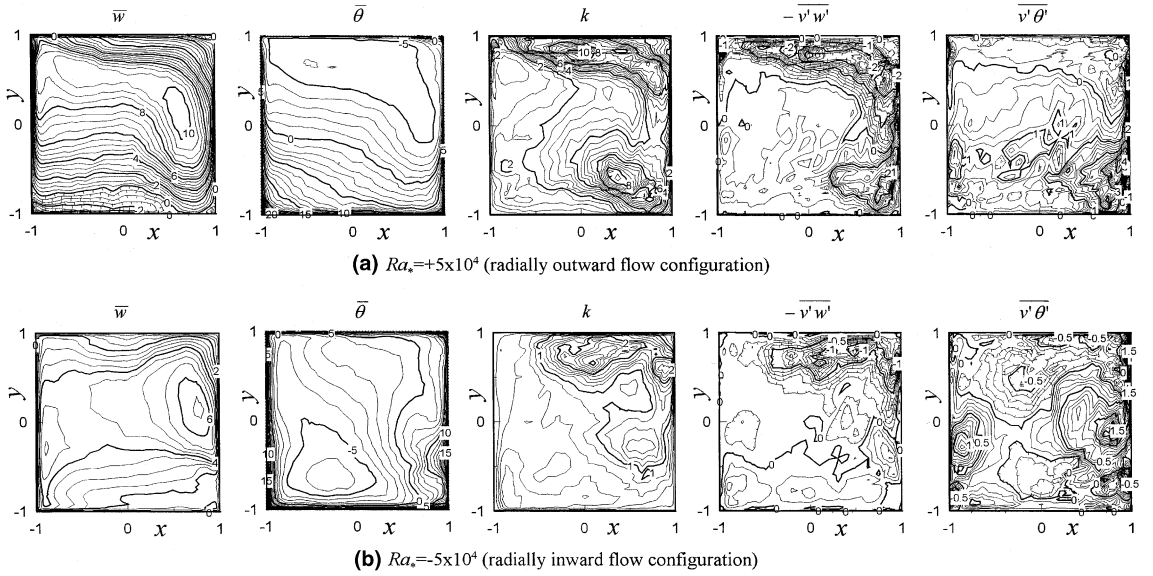

Fig. 9. Isocontours of time-averaged variable sin ξ–η plane at midpoint between ribs (60° rib and $Ro_* = 1$; figures are projected onto x–y plane. The upper and lower walls are the pressure (trailing) and suction (leading) surfaces, respectively. The numbers in each figure show the values for the thick isocontour lines. For k, $-\overline{v'w'}$, and $\overline{v'\theta'}$ in (b), the isocontour lines are drawn doubly dense as compared to those in (a). For, $\bar{w}$, $-\overline{v'w'}$ and $\overline{v'\theta'}$, the isocontour lines for negative values are shown with short projections).

between the ribs and in front of the ribs on the trailing wall. In the 60° rib case, the friction factor decreased with the increase of Gr_m, which was opposite to the results of the 90° rib-roughened and smooth ducts. In the rib-roughened cases, the pressure loss was dominated by the form drag component which was calculated by subtracting the streamwise component of the wall shear stress from the total pressure loss, and the different behavior of the friction factor between the 90° and 60° rib cases was caused by the form drag component. In the 60° rib case, the streamwise velocity and temperature profiles were altered very much by the buoyancy, and the similarity between them and also that between the turbulent statistical values ($-\overline{v'w'}$ and $\overline{v'\theta'}$) broke, because the buoyancy-induced aiding flow enhanced and suppressed the Coriolis induced secondary flow in the radially outward and inward flow configurations, respectively.

References

[1] B. Lakshminarayana, Fluid dynamics and heat transfer of turbomachinery, Wiley, New York, 1996, pp. 597–721 (Chapter 7).

[2] S. Mochizuki, A. Murata, M. Fukunaga, Effects of rib arrangements on pressure drop and heat transfer in a rib-roughened channel with a sharp 180° turn, Trans. ASME J. Turbomachinery 119 (1997) 610–616.

[3] S. Mochizuki, M. Beier, A. Murata, T. Okamura, Y. Hashidate, Detailed measurement of convective heat transfer in rotating two-pass rib-roughened coolant channels, ASME Paper, 96-TA-6, 1996.

[4] A. Murata, S. Mochizuki, T. Takahashi, Local heat transfer measurements of an orthogonally rotating square duct with angled rib turbulators, Int. J. Heat Mass Transfer 42 (1999) 3047–3056.

[5] P.R. Chandra, J.C. Han, S.C. Lau, Effect of rib angle on local heat/mass transfer distribution in a two-pass rib-roughened channel, Trans. ASME J. Heat Transfer 110 (1988) 233–241.

[6] M. Hirota, H. Fujita, H. Yokosawa, T. Nakayama, T. Tanaka, Developing heat/mass transfer in low-aspect-ratio rectangular channels with ribbed walls, in: Proceedings of the 11th International Heat Transfer Conference, Taylor & Francis, London, PA, 1998; Heat Transfer 1998, 5 (1998) 363–368.

[7] G. Rau, M. Cakan, D. Moeller, T. Arts, The effect of periodic ribs on the local aerodynamic and heat transfer performance of a straight cooling channel, ASME Paper 96-GT-541, 1996.

[8] J.W. Baughn, X. Yan, Local heat transfer measurements in square ducts with transverse ribs, Enhanced Heat Transfer ASME HTD-202 (1992) 1–7.

[9] S.V. Ekkad, J.C. Han, Detailed heat transfer distributions in two-pass square channels with rib turbulators, Int. J. Heat Mass Transfer 40 (1997) 2525–2537.

[10] C. Prakash, R. Zerkle, Prediction of turbulent flow and heat transfer in a ribbed rectangular duct with and without rotation, Trans. ASME J. Turbomachinery 117 (1995) 255–264.

[11] M.A. Stephens, T.I-P. Shih, K.C. Civinskas, Effects of inclined rounded ribs on flow and heat transfer in a square duct, AIAA Paper 95-2115, 1995.

[12] B. Banhoff, U. Tomm, B.V. Johnson, Heat transfer predictions for U-shaped coolant channels with skewed ribs and with smooth walls, ASME Paper 96-TA-7, 1996.

[13] B.E. Launder, D.P. Tselepidakis, B.A. Younis, A second-moment closure study of rotating channel flow, J. Fluid Mech. 183 (1987) 63–75.

[14] A. Huser, S. Biringen, Direct numerical simulation of turbulent flow in a square duct, J. Fluid Mech. 257 (1993) 65–95.

[15] S. Gavrilakis, Numerical simulation of low Reynolds number turbulent flow through a straight square duct, J. Fluid Mech. 244 (1992) 101–129.

[16] R.K. Madabhushi, S.P. Vanka, Large eddy simulation of turbulence-driven secondary flow in a square duct, Phys. Fluids A3-11 (1991) 2734–2745.

[17] T. Kajishima, Y. Miyake, T. Nishimoto, Large eddy simulation of turbulent flow in a square duct, Trans. JSME (B) 57–540 (1991) 2530–2537 (in Japanese).

[18] A. Murata, S. Mochizuki, Large eddy simulation with a dynamic subgrid-scale model of turbulent heat transfer in an orthogonally rotating smooth square duct, Int. J. Transport Phenomena 2 (2000) 27–41.

[19] A. Murata, S. Mochizuki, Effect of cross-sectional aspect ratio on turbulent heat transfer in an orthogonally rotating rectangular smooth duct, Int. J. Heat Mass Transfer 42 (1999) 3803–3814.

[20] A. Murata, S. Mochizuki, Large eddy simulation applied to internal forced-convection cooling of gas-turbine blades, in: Proceedings of the 11th International Heat Transfer Conference, Taylor & Francis, London, Heat Transfer 1998, 6 (1998) 565–570.

[21] A. Murata, S. Mochizuki, Large eddy simulation with a dynamic subgrid-scale model of turbulent heat transfer in an orthogonally rotating rectangular duct with transverse rib turbulators, Int. J. Heat Mass Transfer 43 (2000) 1243–1259.

[22] A. Murata, S. Mochizuki, Large eddy simulation of turbulent heat transfer in an orthogonally rotating square duct with angled rib turbulators, Trans. ASME J. Heat Transfer, JHT 99-H-1257, submitted, for publication.

[23] A. Murata, S. Mochizuki, Comparison between laminar and turbulent heat transfer in a stationary square duct with transverse or angled rib turbulators, Int. J. Heat Mass Transfer 44 (2001) 1127–1141.

[24] M.E. Taslim, S.D. Spring, Effect of turbulator profile and spacing on heat transfer and friction in a channel, J. Thermophys. Heat Transfer 8–3 (1994) 555–562.

[25] G.J. Korotky, M.E. Taslim, Rib heat transfer coefficient measurements in a rib-roughened square passage, ASME Paper 96-GT-356, 1996.

[26] J.C. Han, J.S. Park, C.K. Lei, Heat transfer enhancement in channels with turbulence promoters, Trans. ASME J. Eng. Gas Turbines Power 107 (1985) 628–635.

[27] S.V. Patankar, C.H. Liu, E.M. Sparrow, Fully developed flow and heat transfer in ducts having streamwise-periodic

variations of cross-sectional area, Trans. ASME J. Heat Transfer 99 (1977) 180–186.
[28] T. Kajishima, T. Ohta, K. Okazaki, Y. Miyake, High-order finite-difference method for incompressible flows using collocated grid system, JSME Int. J., Series B 41–4 (1998) 830–839.
[29] C. Meneveau, T.S. Lund, W.H. Cabot, A Lagrangian dynamic subgrid-scale model of turbulence, J. Fluid Mech. 319 (1996) 353–385.
[30] P. Moin, K. Squires, W. Cabot, S. Lee, A dynamic subgrid-scale model for compressible turbulence and scalar transport, Phys. Fluids A3-11 (1991) 2746–2757.
[31] F.H. Harlowand, J.E. Welch, Numerical calculation of time-dependent viscous incompressible flow of fluid with free surface, Phys. of Fluids 8–12 (1965) 2182–2189.
[32] J. Kim, P. Moin, Application of a fractional-step method to incompressible Navier–Stokes equations, J. Comp. Phys. 59 (1985) 308–323.
[33] Y. Zang, R.L. Street, J.R. Koseff, A non-staggered grid, fractional step method for time-dependent incompressible Navier–Stokes equations in curvilinear coordinates, J. Comp. Phys. 114 (1994) 18–33.
[34] W.M. Kays, M.E. Crawford, Convective Heat and Mass Transfer, third ed., McGraw-Hill, New York, 1993, p. 316.
[35] M. Nishimura, N. Kasagi, Direct numerical simulation of combined forced and natural turbulent convection in a rotating plane channel, in: Proceedings of the Third KSME–JSME Thermal Engineering Conference, Kyongju, Korea, III (1996) 77–82.
[36] J.H. Wagner, B.V. Johnson, F.C. Kopper, Heat transfer in rotating serpentine passages with smooth walls, Trans. ASME J. Turbomachinery 113 (1991) 321–330.
[37] B.V. Johnson, J.H. Wagner, G.D. Steuber, F.C. Yeh, Heat transfer in rotating serpentine passages with trips skewed to the flow, Trans. ASME J. Turbomachinery 116 (1994) 113–123.